



Photocatalytic hydrogen peroxide production by anthraquinone-augmented polymeric carbon nitride

Hyoung-il Kim^{a,c}, Yeoseon Choi^b, Shu Hu^c, Wonyong Choi^b, Jae-Hong Kim^{c,*}

^a Department of Civil and Environmental Engineering, Yonsei University, Seoul, 03722, Republic of Korea

^b Division of Environmental Science and Engineering, Pohang University of Science and Technology (POSTECH), Pohang, 37673, Republic of Korea

^c Department of Chemical and Environmental Engineering, School of Engineering and Applied Science, Yale University, New Haven, CT, 06511, United States



ARTICLE INFO

Keywords:

Anthraquinone
Electron transfer catalysis
Photosynthesis
Solar fuel
 H_2O_2

ABSTRACT

We describe the exploitation of the selective catalytic property of anthraquinone (AQ) for solar photocatalytic synthesis of hydrogen peroxide (H_2O_2) as a green, sustainable alternative to organic-solvent-based and energy-intensive industry-benchmark processes that also rely on AQ catalysis. We accomplished this by anchoring AQ onto polymeric carbon nitride (C_3N_4), a metal-free visible light photocatalyst (band gap energy = 2.7 eV), that has been previously demonstrated for selective H_2O_2 synthesis. A net H_2O_2 production rate of $361 \mu\text{mol g}^{-1} \text{h}^{-1}$ and an apparent quantum yield (AQY) of 19.5% at 380 nm excitation were achieved using AQ-augmented C_3N_4 under simulated 1-sun illumination in the presence of an organic electron donor (2-propanol); these results were 4.4-fold and 8.3-fold higher than those reported for bare C_3N_4 , respectively. A suite of experimental analyses confirmed the unique roles of AQ co-catalysis in (i) capturing electrons from the conduction band of C_3N_4 , thereby reducing futile exciton recombination, which is otherwise prevalent in bare C_3N_4 ; (ii) effectively mediating electron transfer to drive hydrogenation reaction to form anthrahydroquinone (AQH_2) from AQ; and (iii) catalyzing oxygen reduction to H_2O_2 through the dehydrogenation of AQH_2 back to AQ, resulting in the facile and selective formation of H_2O_2 . In addition, the reduced decomposition of produced H_2O_2 by the $\text{C}_3\text{N}_4/\text{AQ}$ composite photocatalysts, when compared to bare C_3N_4 or C_3N_4 composites with common metallic co-catalysts such as Pt and Ag, was found to contribute to the significant enhancement in H_2O_2 production through the oxidation of both organic and water.

1. Introduction

Hydrogen peroxide (H_2O_2) is a widely used commodity chemical with an estimated global gross production of 3 million metric tons per year [1]. It is an environmentally friendly and easy-to-handle oxidant, since it generates only water and oxygen after its use. Due to a relatively high oxidation potential ($E_0 = 1.763 \text{ V vs. NHE at pH } 0$), H_2O_2 can oxidize a variety of organic and inorganic substrates through facile liquid- or vapor-phase reactions [2]. These unique properties allow H_2O_2 to function in a broad range of industrial and commercial applications in the chemical production, medical practice, and environmental remediation. In particular, a large quantity of H_2O_2 is used in the advanced oxidation process in water and wastewater treatment as a precursor for producing hydroxyl radicals via UV irradiation and catalyst (e.g., reduced Fe and Cu) activation [3,4].

H_2O_2 is also considered an alternative liquid fuel with higher energy density than compressed H_2 gas (200 psi). Concentrated H_2O_2 has been used as a liquid fuel for propulsion and actuation [5]. Chemical energy

stored in H_2O_2 can be converted to electricity on demand via a H_2O_2 fuel cell [6,7], or to H_2 by applying a small voltage ($\sim 0.6 \text{ V}$). The exhaust from either process does not produce greenhouse gases, but only oxygen and water. Up to a 0.8 V open-circuit voltage has been reported with H_2O_2 fuel cells, which rivals state-of-the-art H_2 fuel cells [8]. Despite established industrial use as well as growing interest in both environment and energy sectors, the current H_2O_2 production technology is energy- and chemical-intensive and far from being carbon neutral within its life cycle, significantly limiting its sustainable growth.

Solar-driven photocatalytic production of H_2O_2 has been emerging as an environmentally friendly and sustainable alternative because its production requires only sunlight, water, and air [9,10]. At present, the most common H_2O_2 production process is based on the anthraquinone (AQ) method, also referred to as the Riedl-Pfleiderer process, which involves hydrogenation and auto-oxidation as the first two steps (Fig. S1) [11]. In the first step, hydrogenation, 2-alkyl-anthraquinone (R-AQ) is hydrogenated catalytically to alkyl-anthrahydroquinone (R-AQH₂) by reacting with H_2 on a catalyst surface in a solvent (e.g., trioctyl

* Corresponding author.

E-mail address: jaehong.kim@yale.edu (J.-H. Kim).

phosphate and trimethyl benzene). In the second step, oxidation, the hydrogenated R-AQH₂ is oxidized by oxygen (typically by oxygen in air) to revert to R-AQ with the concurrent H₂O₂ production. Although this industry standard process achieves relatively high H₂O₂ yields due to AQ's exceptional selectivity toward H₂O₂-evolving reactions, it requires costly hydrogen gas and noble metals, toxic organic solvents, and a large energy input to provide the necessary high temperature [12]. Alternative processes which can directly synthesize H₂O₂ on metal catalysts (e.g., Pd or Pd/Au alloys) from the hydrogen and oxygen gas have been explored, but these processes require a large amount of energy and also face the risk of explosion of the H₂/O₂ gaseous mixture [13,14].

Polymeric carbon nitride (C₃N₄) has been considered one of the most suitable photocatalysts to achieve this goal for several reasons. First, C₃N₄ is metal free and exhibits superior stability and excellent optical absorption of visible light. It can be readily synthesized by the heat-induced polymerization of various precursors such as melamine and therefore is relatively inexpensive [15]. Second, unlike metal oxide semiconductors [16], C₃N₄ not only catalyzes water-splitting (1.8 vs. RHE and -0.9 vs. RHE for the valence band and conduction band, respectively) [17] but also exhibits selectivity towards H₂O₂ production through the sequential formation of a superoxo radical and 1,4-endoperoxide species [18,19]. Third, C₃N₄ exhibits relatively narrow bandgap energy (2.6–2.7 eV) compared to most UV absorbers like TiO₂, allowing it to utilize the visible portion of the solar spectrum. Note that co-catalysts are commonly used with small-bandgap photocatalysts (< 2.7 eV) to improve rates of charge transfer and multi-electron catalysis and to prevent rapid recombination of excited charges or excitons by charge separation; noble metals and carbon materials (e.g., Au [20], Au–Ag [21], Au–Pd [22], graphene [9], graphene oxide (GO) [23], reduced GO (rGO) [24]) are benchmark co-catalysts due to their ability to withdraw electrons from conduction bands and transfer them to electron acceptors. However, these co-catalysts either decompose H₂O₂ or exhibit poor selectivity towards the selective 2-electron reduction of O₂ to H₂O₂.

We present here a new approach that leverages the exceptional activity and selectivity of AQ chemistry for reductive H₂O₂ synthesis using C₃N₄ particles as a visible light absorber. Different from the industrial process, the molecular AQ catalysts are augmented onto heterogeneous surfaces of C₃N₄ particles such that AQ chemistry can be solar-driven (**Scheme 1**). In this mechanism, AQ withdraws electrons from the C₃N₄ conduction band such that (1) AQ functions as a co-catalyst to minimize charge recombination and ultimately enhance the quantum yield, overcoming the limitation of small-bandgap photocatalysts [25]; and (2) AQ transfers electrons to initiate the electron-coupled hydrogenation reaction (AQ to AQH₂) with a low-lying reduction potential (0.1 V vs. NHE) [26]. Subsequently, H₂O₂ is synthesized as oxygen is reduced through the dehydrogenation reaction of AQH₂ to AQ. C₃N₄ is particularly instrumental for this composite material approach since N sites of C₃N₄ offer a molecular handle for grafting AQ molecules. We successfully synthesized AQ-augmented C₃N₄ (in this study termed C₃N₄/AQ) and performed various photo (electro)chemical characterizations to demonstrate highly efficient photocatalytic H₂O₂ generation at a production rate of 361 μmol g⁻¹ h⁻¹. This rate is a 4.4-fold higher value than that of bare C₃N₄ (82.3 μmol g⁻¹ h⁻¹) under simulated solar illumination.

2. Experiments

2.1. Synthesis of C₃N₄ photocatalysts

A batch of C₃N₄ was prepared by heating melamine (99%, Aldrich) at 550 °C, which was reached at a ramp rate of 2.5 °C min⁻¹, for 3 h in an alumina boat crucible covered with a lid. After cooling to RT, the collected sample was suspended in DI water. Unreacted melamine was removed by filtering the suspension (Supor®, 0.45 μm, Pall

Corporation) and washed with DI water several times. The purified C₃N₄ was dried at 70 °C overnight for further use. Melem was prepared by the same process except that the temperature was raised to 425 °C at 2.5 °C min⁻¹ and kept for 6 h.

2.2. Synthesis of AQ-augmented C₃N₄ composite

AQ-augmented C₃N₄ was prepared through the catalyst-free direct coupling method [27]. As-prepared C₃N₄ (0.2 g) was suspended in 18 mL of acetonitrile (99.8%, Aldrich) and a varying amount (1–20 wt% with respect to C₃N₄) of anthraquinone-2-carboxylic acid (AQ-COOH, 98%, Aldrich) was added to the suspension. The suspension was sonicated for 30 min and stirred for 12 h at 50 °C. After cooling down to RT, the suspension was filtered (Supor®, 0.45 μm, Pall Corporation), washed several times with DI water and ethanol to remove remaining AQ-COOH, and dried overnight at 70 °C. Composites of C₃N₄ with AQ derivatives with different functional groups (2-aminoanthraquinone, Aldrich), sodium anthraquinone-2-sulfonate (≥ 98%, Aldrich), and 2-(hydroxymethyl)anthraquinone (97%, Aldrich)) were also prepared following the same synthetic procedure. AQ-augmented melem (melem/AQ) was prepared by the same procedure as for C₃N₄/AQ, but substituting melem for C₃N₄.

2.3. Synthesis of C₃N₄ composite with metal co-catalysts

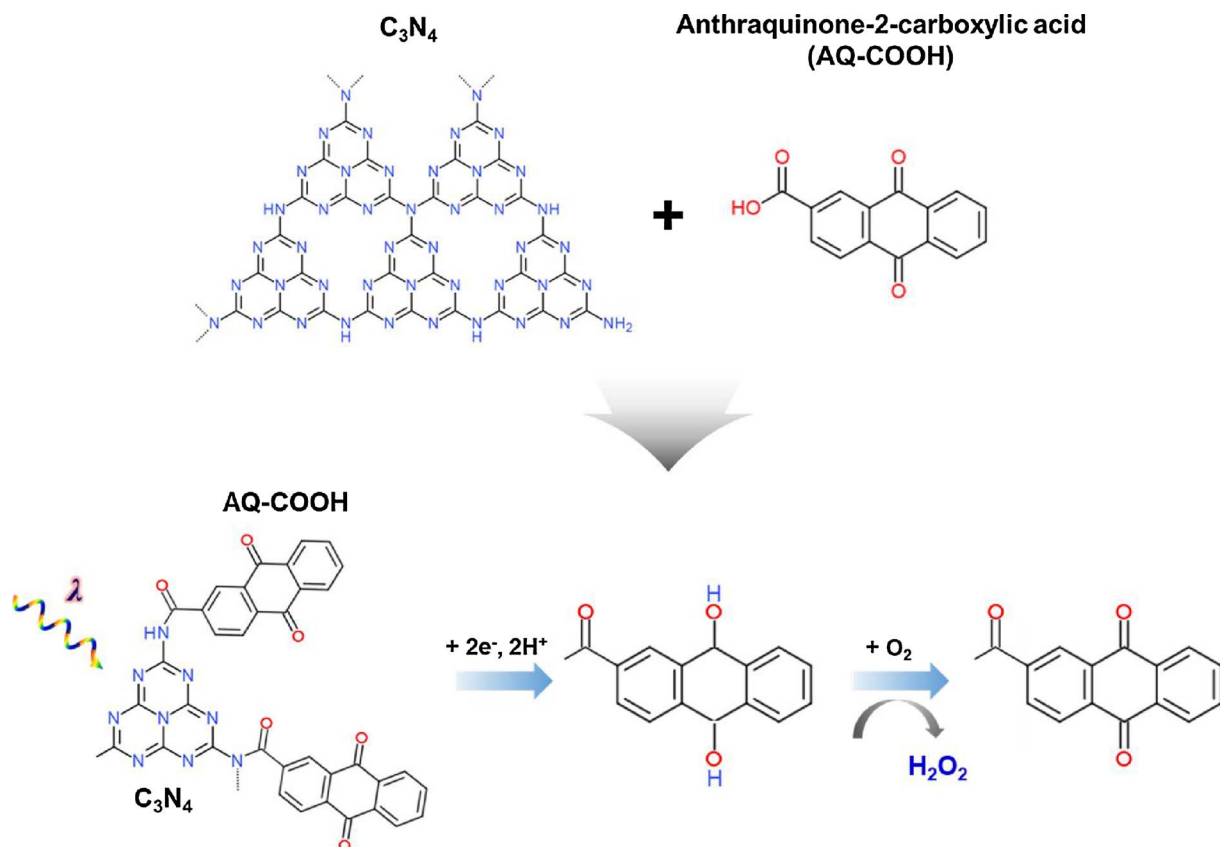
Composites of C₃N₄ with various noble metal co-catalysts were prepared via a well-established photo-deposition method [28] using hydrogen tetrachloroaurate trihydrate (HAuCl₄·3H₂O, ≥ 99.9%, Aldrich), chloroplatinic acid hexahydrate (H₂PtCl₆·6H₂O, Aldrich), and silver nitrate (AgNO₃, ≥ 99.0%, Aldrich) as metal precursors. An aqueous suspension containing C₃N₄, one of these metal precursors, and an electron donor (10 vol% methanol) was irradiated by a white LED (100 W) for 4 h for photo-deposition of the respective metal co-catalysts.

2.4. Synthesis of C₃N₄ composite with carbon co-catalysts

C₆₀ (1 wt%)-loaded C₃N₄ was prepared following the previously established procedure with a slight modification [29]. The melamine (1 g) and C₆₀ (0.5 or 10 mg, SES Research, 99.9%) were first grounded together using mortar and pestle for 10 min. The mixture was then placed in an alumina boat crucible covered with a lid and heated at 550 °C for 3 h following the same procedure for bare C₃N₄ synthesis. C₃N₄ was also loaded with GO and rGO (10 wt%), prepared by the modified Hummers method and by further reducing GO with hydrazine [30], respectively. The GO or rGO suspension (2.0 mg/mL) was added to the aqueous suspension of C₃N₄ that had been ultrasonicated for 3 h to exfoliate C₃N₄. This mixture was further ultrasonicated for 3 h, vigorously stirred for additional 6 h, washed with DI water, and dried at 80 °C overnight.

2.5. Characterization

The crystalline phases of C₃N₄ and modified C₃N₄ samples were analyzed using a powder X-ray diffraction (XRD) with Cu Kα radiation (MAC Science, M18XHF). Diffuse reflectance spectra (DRS) were obtained using a Varian Cary 3 spectrophotometer equipped with an integrating sphere, and their band gaps were estimated using Tauc's plot. X-ray photoelectron spectroscopy (XPS) analysis was performed using a Theta Probe AR-XPS System (Thermo Fisher Scientific) with a monochromatic Al Kα source (1486.6 eV). Fourier transform infrared (FT-IR) spectra were obtained using a Thermo Scientific Nicolet 6700 FT-IR spectrometer.



Scheme 1. Schematic illustration of the process to couple C_3N_4 with AQ-COOH and the photocatalytic hydrogen peroxide generation process by AQ-COOH-coupled C_3N_4 under solar light irradiation.

2.6. Photocatalytic H_2O_2 production

Photocatalytic H_2O_2 production experiments were carried out by irradiating simulated solar light (AM 1.5, 100 mW cm⁻²) from a 150-W Xenon Arc lamp to the aqueous suspension of 0.5 g/L of differently modified C_3N_4 containing 2-propanol (10 vol%) as an electron donor. The suspension was continuously purged with O_2 for 20 min before and during illumination. The incident light intensity was determined using a Newport calibrated Si solar cell. The concentration of produced H_2O_2 was colorimetrically determined using titanium(IV) sulfate (30% Solution, Fisher Scientific) that forms pertitanic acid (H_2TiO_4) upon reaction with H_2O_2 [31]. Briefly, a sample aliquot was collected from the reaction suspension using a syringe, filtered through a syringe filter (0.45 µm PTFE, Pall), and mixed with a titanium (IV) sulfate solution (0.64%, diluted by sulfuric acid). The absorbance at λ_{max} (405 nm) of pertitanic acid in the mixture was monitored using a UV-visible spectrophotometer ($\epsilon = 730 \text{ M}^{-1} \text{ cm}^{-1}$) [31]. A DPD (N,N diethyl-1,4 phenylenediamine sulfate) colorimetric method ($\epsilon = 21,000 \text{ M}^{-1} \text{ cm}^{-1}$) [10,32] was also used for the samples with relatively low H_2O_2 concentration ($100 \leq \mu\text{M}$). Apparent quantum efficiency (AQY) was characterized by illuminating the suspension of C_3N_4 and $\text{C}_3\text{N}_4/\text{AQ}$ in the presence of 2-propanol electron donor with monochromated light ($\lambda = 380, 400, 420, 450$, and 480 nm) through bandpass filters (Thorlabs).

2.7. Photoelectrochemical characterization

Photoelectrochemical (PEC) characterizations were conducted using a conventional three-electrode potentiostat setup connected to a Gamry potentiostat (Reference 600). The PEC reactor consisted of two coiled Pt wires and a saturated Ag/AgCl/KCl (sat) electrode as working, counter, and reference electrodes, respectively. The photocurrent derived from photo-generated charge carriers on photocatalysts was collected on a Pt

working electrode (at 1.1 V vs. RHE (0.8 V vs. Ag/AgCl)) through $\text{Fe}^{3+}/\text{Fe}^{2+}$ electron shuttles (0.2 mM) in the photocatalyst suspension (0.5 g L^{-1} , $[\text{NaClO}_4] = 0.1 \text{ M}$, $\text{pH}_i = 1.8$) under simulated solar illumination (AM 1.5, 100 mW cm⁻²). Electrochemical (EC) characterization was performed in a PEC reactor that consisted of a glassy carbon electrode (GCE, CH Instruments (CHI104), 3.0 mm diameter), a coiled Pt wire, and a saturated Ag/AgCl/KCl (sat) electrode as working, counter, and reference electrodes, respectively. The GCE was loaded with photocatalysts fabricated by first mixing catalysts (10 mg) with Nafion resin binder (60 µL, 5 wt% Alfa Aesar Nafion perfluorinated resin in a mixture of water and 1-propanol), further dissolving the mixture in 2-propanol (800 µL), depositing the final mixture onto the electrode and drying at RT, and further drying at 105 °C overnight. Cyclic voltammograms (CVs) and linear sweep voltammograms (LSVs) were obtained at a scan rate of 50 mV s⁻¹ over a range of potentials (from -1.2 to +1.0 vs. Ag/AgCl for CV and from -1.1 to +0.6 V vs. Ag/AgCl for LSV). Electrochemical impedance spectroscopy (EIS) analysis was performed at a DC voltage of -0.5 V vs. Ag/AgCl, an AC voltage amplitude of 50 mV, and a frequency ranging from 500 mHz to 100 kHz.

3. Results and discussion

3.1. Characterization of $\text{C}_3\text{N}_4/\text{AQ}$

A successful synthesis of C_3N_4 from melamine was first confirmed by XRD, UV-vis, and FT-IR absorption spectral analyses (Fig. 1). When the reaction synthesis reached around 425 °C, we observed the formation of a condensed carbon nitride compound, melem ($\text{C}_6\text{N}_7(\text{NH}_2)_3$), as indicated by a typical monoclinic unit cell XRD diffraction pattern (Fig. 1a; see Fig. S2 for the reaction scheme) [33]. Further reaction at a higher temperature (550 °C) leads to additional condensation and

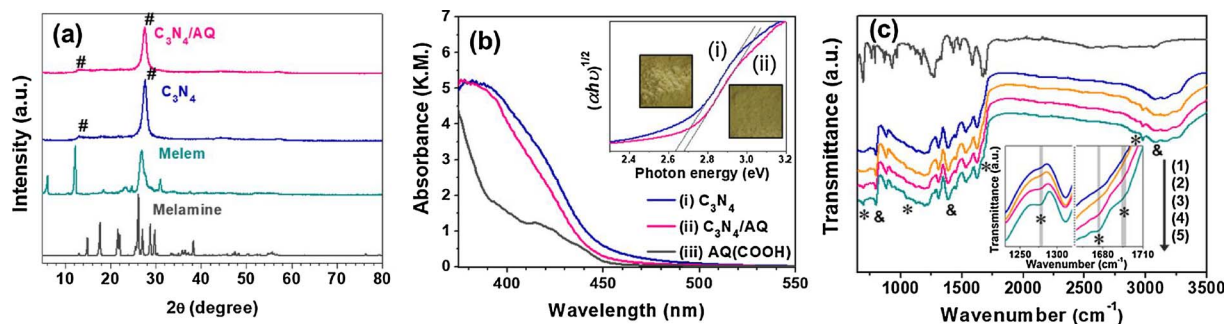


Fig. 1. (a) XRD spectra of melamine, melem, C₃N₄, and C₃N₄/AQ(-COOH). ‘#’ in (a) represents two main diffraction peaks (13.0° (100) and 27.4° (002)) of C₃N₄ [34]. Absorption intensities in (b) were expressed in the Kubelka-Munk unit (KM = $(1 - R^2)/2R$). The inset in (b) shows the photographs and the estimated band gaps (using Tauc’s plot) of C₃N₄ and C₃N₄/AQ(-COOH), assuming indirect transitions. (c) FT-IR spectra of (1) AQ(-COOH), (2) C₃N₄, (3) C₃N₄/AQ (5 wt%), (4) C₃N₄/AQ (10 wt%), and (5) C₃N₄/AQ (20 wt%). The inset in (c) shows the magnified FT-IR spectra in the range between 1230 and 1320 cm⁻¹ and between 1660 and 1710 cm⁻¹, respectively. Notations ‘&’ and ‘*’ in (c) represent main absorption peaks of C₃N₄ and AQ induced absorption peaks on C₃N₄/AQ, respectively.

formation of C₃N₄, one of the most stable allotropes of carbon nitride, that consists of tri-s-triazine (C₆N₇) units as evidenced by the XRD peak at 27.4° (002) [34]. The band-edge wavelength of the C₃N₄ was at 470 nm (Fig. 1b), which corresponds to band gap energy (E_{BG}) of ca. 2.64 eV according to Tauc’s plots (Fig. 1b inset, $(ahv)^{1/2} \propto (hv - E_g)$) and confirms C₃N₄’s visible light absorption capability [25,35]. The FT-IR spectrum of C₃N₄ (Fig. 1c) was characterized by the triazine unit’s breathing mode peak at 798 cm⁻¹ as well as a skeletal stretching mode peak of C–N at 1250–1420 cm⁻¹ and C=N bonds at 1550–1630 cm⁻¹, respectively [36,37]. Broad absorption peaks at 3050–3400 cm⁻¹ belong to edge amino groups (–NH/NH₂) [37,38].

The crystal structure of C₃N₄ was not affected by AQ coupling, as evidenced by the XRD spectrum where only slight broadening of main diffraction peaks (13.0° (100) and 27.4° (002)) was observed (Fig. 1a). The band-edge wavelength appeared slightly blue-shifted by 10 nm, and E_{BG} marginally increased to 2.68 eV from 2.64 eV after coupling with AQ (Fig. 1b). This minor change is attributed to AQ(-COOH)’s lower absorbance and narrower absorption band than C₃N₄, as the spectrum reflects the mixed absorption of C₃N₄ and AQ(-COOH). The result suggests that there is no direct optical transition between C₃N₄ and AQ. In contrast, we observed a gradual change in FT-IR spectra with increasing AQ(-COOH) contents (Fig. 1c). Peaks centered at 698 cm⁻¹ and 2974 cm⁻¹, corresponding to C–H bending and stretching vibrations from AQ, respectively, confirm AQ coupling [39,40]. The increase in absorption at 1278 cm⁻¹ and 1676 cm⁻¹, corresponding to C–N stretching and carbonyl C=O stretching vibrations, respectively, indicates the amide bond formation [41,42]. However, the separate absorption band of amide N–H vibrations at 3320 cm⁻¹ was not observed, due to the overlap with the broad absorption of uncondensed amine groups (3050–3400 cm⁻¹) [38,42,43].

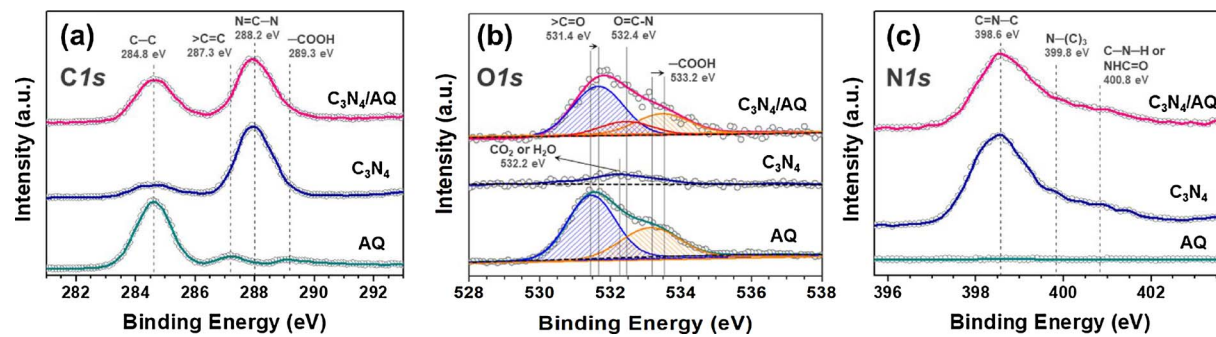
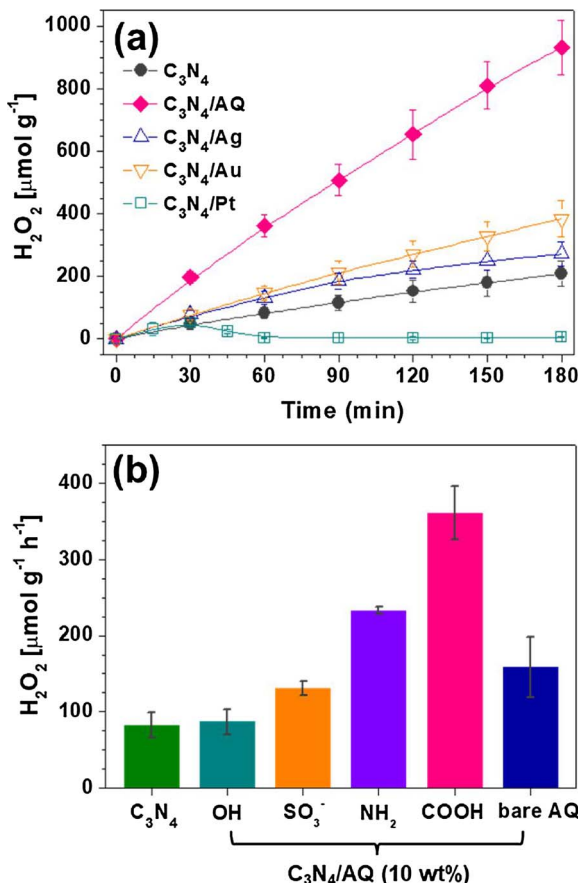
XPS analysis provided clearer evidence of the covalent bonding of AQ-COOH to C₃N₄. In the C1s spectrum, C₃N₄ showed a weak peak at a binding energy of 284.8 eV and a prominent peak at 288.2 eV; these peaks are assigned to the C–C bonding of surface adventitious carbon/defect-derived sp²-carbon and the N–C=N bond in the triazine units, respectively (Fig. 2a) [44]. When coupled with AQ, a strong aromatic C–C bonding peak at 284.8 eV, originating from AQ, emerged from the background of adventitious carbon [45]. In the O1s spectra, AQ coupling resulted in the decrease and shift (toward higher energy) of the COOH peak at 533.2 eV and >C=O peak at 531.4 eV, concurrent with formation of the amide bond (O=C–N, at 532.4 eV) from the reaction between –COOH in AQ and –NH₂ in C₃N₄ (Fig. 2b) [45,46]. The weak peak at 532.2 eV on C₃N₄ is attributed to adsorbed CO₂ or H₂O on the surface [47]. In N1s spectra, both C₃N₄ and C₃N₄/AQ displayed a similar shape composed of three major peaks at ca. 398.6, 399.8, and 400.8 eV; the peak shape corresponds to sp²-hybridized aromatic N in the form of C=N–C, the ternary N–(C)₃ groups, and the sp³-hybridized amino functional groups, respectively (Fig. 2c) [48]. However,

the peak for amide that forms as a result of the reaction between AQ and C₃N₄ was indistinguishable from the peak for amino functional groups of C₃N₄. Collectively, these results indicate that AQ molecules were successfully augmented to C₃N₄ without significant structural changes by the simple heat-induced hybridization procedure.

3.2. Photocatalytic H₂O₂ production by C₃N₄/AQ

Results shown in Fig. 3a and summarized in Table 1 suggest that C₃N₄ photocatalytically produces H₂O₂ under solar-simulated light illumination, and the rate of production is faster when C₃N₄ is coupled with AQ compared to other commonly used co-catalysts (refer to Figs. S3 and S4 for their properties). The noble metals such as Ag, Au, and Pt deposited onto the photocatalyst function as co-catalysts, promoting interfacial electron transfer from the conduction band of C₃N₄ to the electron acceptor and thereby reducing futile exciton recombination [49,50]. Accordingly, H₂O₂ production increased by approximately 60% and 80% (from 82.3 to 132 and 147 μmol g⁻¹ h⁻¹) by Ag and Au loading, respectively. In contrast, carbon-based co-catalysts (C₆₀, GO, and rGO) were detrimental to H₂O₂ production (H₂O₂ production rate reduced by 32%, 24%, and 10% with C₆₀ (1 wt%), GO (10 wt%), and rGO (10 wt%), respectively), presumably due to accelerated single-electron transfer to oxygen leading to the formation of superoxide radical anion, instead of forming H₂O₂ through two-electron transfer [51,52].

When C₃N₄ was coupled with AQ (10 wt%), the H₂O₂ production rate was significantly increased to a rate 4.4 times higher than that of bare C₃N₄, from 82.3 to 361 μmol g⁻¹ h⁻¹. The kinetic enhancement was dependent on the amount of AQ loaded onto C₃N₄; the maximum rate was achieved at 10 wt% (Fig. S5). The decrease in the H₂O₂ production rate at higher AQ loading is likely to have resulted from the light shielding, as the absorption of AQ overlaps with C₃N₄ in the UV region. Similar observations have been reported for other carbon-based co-catalysts such as carbon nanotubes, GO, and rGO [53,54]. These results suggest AQ plays a critical role in significantly enhancing production of H₂O₂ via photocatalysis. We found that the H₂O₂ production rate was also enhanced when AQ was physisorbed onto C₃N₄; a strong physisorption is expected through π–π interaction between basal planes of AQ and C₃N₄, similar to the interaction between AQ and graphene [55]. AQ derivatives with different functional groups, such as -OH, -SO₃⁻, -NH₂ instead of -COOH or without a functional group (bare AQ), all enhanced H₂O₂ production but to a much lesser extent than when AQ(-COOH) was grafted to C₃N₄ via amide bonding (Fig. 3b). Although π–π interaction between C₃N₄ and AQ(-COOH) cannot be ruled out, this chemical grafting in C₃N₄/AQ(-COOH) appeared necessary not only to bind AQ securely onto the photocatalyst to prevent co-catalyst detachment over time but also to more effectively utilize AQ chemistry.

Fig. 2. XPS spectra of (a) C1s, (b) O1s, and (c) N1s on AQ(-COOH), C₃N₄, and C₃N₄/AQ(-COOH) (10 wt%).Fig. 3. (a) Time-dependent profiles of H₂O₂ production by C₃N₄, C₃N₄/AQ(-COOH), and C₃N₄/(Ag, Au, Pt) metals (1 wt%) with 2-propanol as the electron donor. (b) H₂O₂ production as a function of anchoring groups of AQ molecules on C₃N₄/AQ (after 1 h reaction). The experimental conditions were as follows: [catalyst] = 0.5 g L⁻¹, [2-propanol]₀ = 10 vol%, pH_i = not adjusted, 100 mW cm⁻² (AM 1.5), and O₂-saturated.

3.3. Mechanism of AQ co-catalysis

The occurrence of C₃N₄-driven AQ chemistry in the C₃N₄/AQ composite is manifested by the fact that a saturated AQ solution (30 μM) under otherwise identical conditions (e.g., [2-propanol]₀ = 10 vol%, O₂-saturated, 100 mW cm⁻² irradiation by solar simulator) produced a negligible amount of H₂O₂ (Fig. S6). A photocatalytic H₂O₂ generation by AQ alone under UV irradiation is, in fact, possible through the electron transfer mediation by excited triplet-state of AQ to oxygen [56], but such generation is much less efficient compared to the proton-coupled electron transfer (PCET) that occurs on C₃N₄/AQ [57]. Negligible production of H₂O₂ on C₃N₄/AQ in the absence of O₂ (under N₂-saturated condition; Fig. S7b) also supports the finding that AQ functions as a catalyst, not as a reactant. Accordingly, repeated use of C₃N₄/AQ resulted in a negligible

Table 1
Photocatalytic production of H₂O₂ with various modified g-C₃N₄.

Samples	Produced H ₂ O ₂ ^a (μmol g ⁻¹ h ⁻¹)	k _f ^b (μmol g ⁻¹ min ⁻¹)	k _d ^c ((×10 ⁴) min ⁻¹)
g-C ₃ N ₄	82.3 ± 16.5	1.18 ± 0.04	3.89 ± 0.08
g-C ₃ N ₄ /AQ-COOH	361 ± 35.4	5.22 ± 0.13	1.83 ± 0.12
g-C ₃ N ₄ /AQ-OH	86.9 ± 16.6	1.33 ± 0.05	3.12 ± 0.13
g-C ₃ N ₄ /AQ-SO ₃ ⁻	131 ± 9.43	2.33 ± 0.07	5.79 ± 0.37
g-C ₃ N ₄ /AQ-NH ₂	233 ± 4.24	3.63 ± 0.11	2.34 ± 0.15
g-C ₃ N ₄ /AQ	158 ± 39.6	2.62 ± 0.02	3.34 ± 0.12
g-C ₃ N ₄ /Pt (1 wt%)	103 ± 10.4	2.46 ± 0.05	252 ± 10.5
g-C ₃ N ₄ /Ag (1 wt%)	132 ± 19.8	1.64 ± 0.13	10.4 ± 0.16
g-C ₃ N ₄ /Au (1 wt%)	147 ± 22.2	2.22 ± 0.04	5.06 ± 0.19
g-C ₃ N ₄ /C60 (0.05 wt%)	63.2 ± 6.54	1.04 ± 0.05	3.21 ± 0.41
g-C ₃ N ₄ /C60 (1 wt%)	56.0 ± 13.2	0.98 ± 0.01	2.73 ± 0.02
g-C ₃ N ₄ /GO (10 wt%)	62.3 ± 13.6	1.09 ± 0.05	3.78 ± 0.09
g-C ₃ N ₄ /rGO (10 wt%)	74.3 ± 17.4	1.18 ± 0.04	3.28 ± 0.14
Melem	74.0 ± 3.78	1.03 ± 0.04	5.66 ± 0.59
Melem/AQ-COOH	315 ± 29.2	4.49 ± 0.13	2.89 ± 0.50

^a Production rate was estimated by fitting the data (for initial 1 h except C₃N₄/Pt (1 wt %)).

^b k_f (μmol g⁻¹ min⁻¹).

^c k_d ((×10⁴) min⁻¹) were evaluated by assuming the zero-order and first-order kinetics, respectively, through the eqn. of $\left[\frac{H_2O_2}{H_2O_2} \right] = \frac{k_f}{k_d} \{1 - \exp(-k_d t)\}$. All values of C₃N₄/Pt (1 wt%) were evaluated with H₂O₂ production rate for the initial 30 min.

change in photocatalytic properties (Fig. S8). We also observed that the effect of oxygen concentration on H₂O₂ production was less profound for C₃N₄/AQ than bare C₃N₄ (i.e., 16% reduction with C₃N₄/AQ compared to 30% reduction with bare C₃N₄ when the suspension was air-saturated instead of O₂-saturated), suggesting improved oxygen reduction ability through AQ co-catalysis (Fig. S7a and b). Collectively, these results indicate that the main role of AQ in C₃N₄/AQ is co-catalysis leading to accelerated H₂O₂ production from photo-excited C₃N₄.

The enhanced H₂O₂ production by AQ resulted not only from increased H₂O₂ formation but also from reduced H₂O₂ decomposition that occurs through both reductive and oxidative pathways [9]. We separately evaluated the formation (k_f; μmol g⁻¹ min⁻¹) and decomposition (k_d; min⁻¹) rate constants of H₂O₂ using the following equation [58,59]:

$$\left[\frac{H_2O_2}{H_2O_2} \right] = \frac{k_f}{k_d} \{1 - \exp(-k_d t)\} \quad (1)$$

Values of k_f and k_d obtained by fitting the data in Fig. 3a (photocatalytic H₂O₂ production) and Fig. 4a (decomposition of H₂O₂ externally added to the catalyst suspension) to Eq. (1) are summarized in Fig. 4b and Table 1. All C₃N₄ modified with noble metals exhibited the increased k_f values up to 2.1 times (2.46 μmol g⁻¹ min⁻¹ for C₃N₄/Pt) compared to that of bare C₃N₄ (1.18 μmol g⁻¹ min⁻¹). But at the same time, k_d values also increased, from 1.3 to 65 times (0.0252 min⁻¹ for C₃N₄/Pt) compared to that of bare C₃N₄ (0.0004 min⁻¹).

Significant decomposition of H₂O₂ by Pt explains why Pt co-catalyst was not at all effective in enhancing H₂O₂ production. In the case of

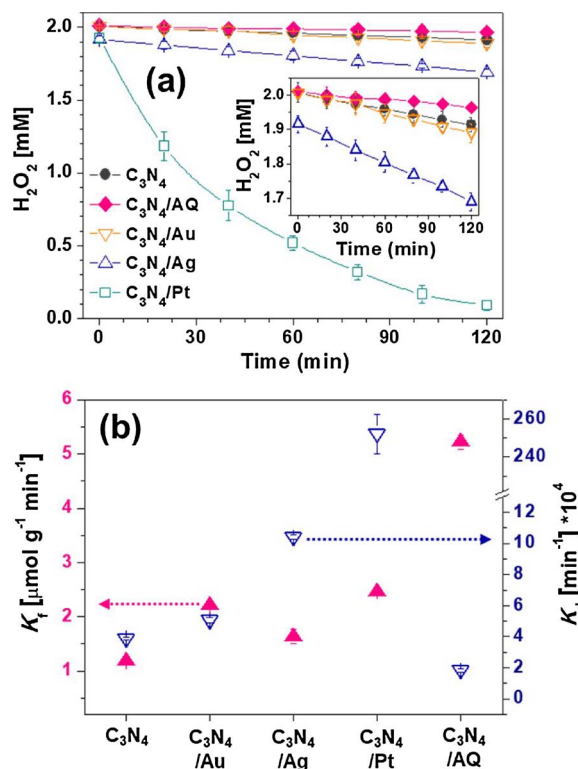


Fig. 4. (a) Time-dependent profiles of photocatalytic decomposition of H₂O₂ ($C_0 = 2$ mM) by C₃N₄, C₃N₄/AQ(-COOH) (10 wt%), and C₃N₄/(Ag, Au, Pt) metals (1 wt%). The inset shows the magnified time-dependent profiles of photocatalytic decomposition of H₂O₂ ($C_0 = 2$ mM) by C₃N₄, C₃N₄/AQ(-COOH) (10 wt%), and C₃N₄/(1 wt%) metals (Ag, Au). (b) Formation rate constants (k_f , filled symbols) and decomposition rate constants (k_d , open symbols) for H₂O₂. The experimental conditions were as follows: [catalyst] = 0.5 g L⁻¹, [H₂O₂] = 2 mM, pH_i = not adjusted, 100 mW cm⁻² (AM 1.5), and O₂-saturated.

C₃N₄/AQ, the k_f value was the greatest at $5.22 \pm 0.13 \mu\text{mol g}^{-1} \text{min}^{-1}$, and the k_d value was the smallest at 0.0002 min^{-1} , accounting for the highest overall efficiency for H₂O₂ production. The effective co-catalysis by AQ was also found by selective O₂ reduction (leading to H₂O₂ formation) instead of O₂ reduction to water or H⁺ to H₂ formation, especially when compared to noble metal co-catalysts. The reduction potential for the formation of H₂O₂ (O₂ + 2H⁺ + 2e⁻ → H₂O₂, $E^0 = 0.695$ V) occurs with a greater thermodynamic driving force than that of H₂ formation (2H⁺ + 2e⁻ → H₂, $E^0 = 0$ V) [60]. Since the photocatalytic H₂O₂ formation can also be initiated by one-electron transfer reactions (O₂ + e⁻ → O₂[•], $E^0 = -0.33$ V; O₂ + H⁺ + e⁻ → HO₂[•], $E^0 = -0.046$ V) [60], both the H₂O₂ and H₂ formation occur competitively in the C₃N₄ photocatalytic system. We observed that, under simulated solar irradiation, noble metal-loaded C₃N₄ produced a significant amount of H₂, for example, at a rate of $92.9 \pm 4.6 \mu\text{mol g}^{-1} \text{h}^{-1}$ for C₃N₄/Pt and $81.9 \pm 3.4 \mu\text{mol g}^{-1} \text{h}^{-1}$ for C₃N₄/Au, while bare C₃N₄ and C₃N₄/AQ produced a negligible amount of H₂ (Fig. S9). This selectivity toward oxygen reduction through PCET explains the overall high efficiency of C₃N₄/AQ in H₂O₂ production.

In the absence of an organic electron donor (i.e., isopropanol), the co-catalytic activity of AQ was more clearly observed where water was used as an electron donor (2H₂O → 4H⁺ + 4e⁻ + O₂) (Fig. S7 a and b). C₃N₄ showed a negligible H₂O₂ production in the absence of an organic electron donor. A small amount of H₂O₂ was produced at an early stage, but it quickly disappeared due to the decomposition of H₂O₂ by C₃N₄. In contrast, C₃N₄/AQ was able to produce H₂O₂ continuously during the 3 h reaction (ca. $110 \mu\text{mol g}^{-1}$). Long-term tests more obviously demonstrated the superior H₂O₂ production by C₃N₄/AQ using water as the electron donor (Fig. S7c). These results collectively support the

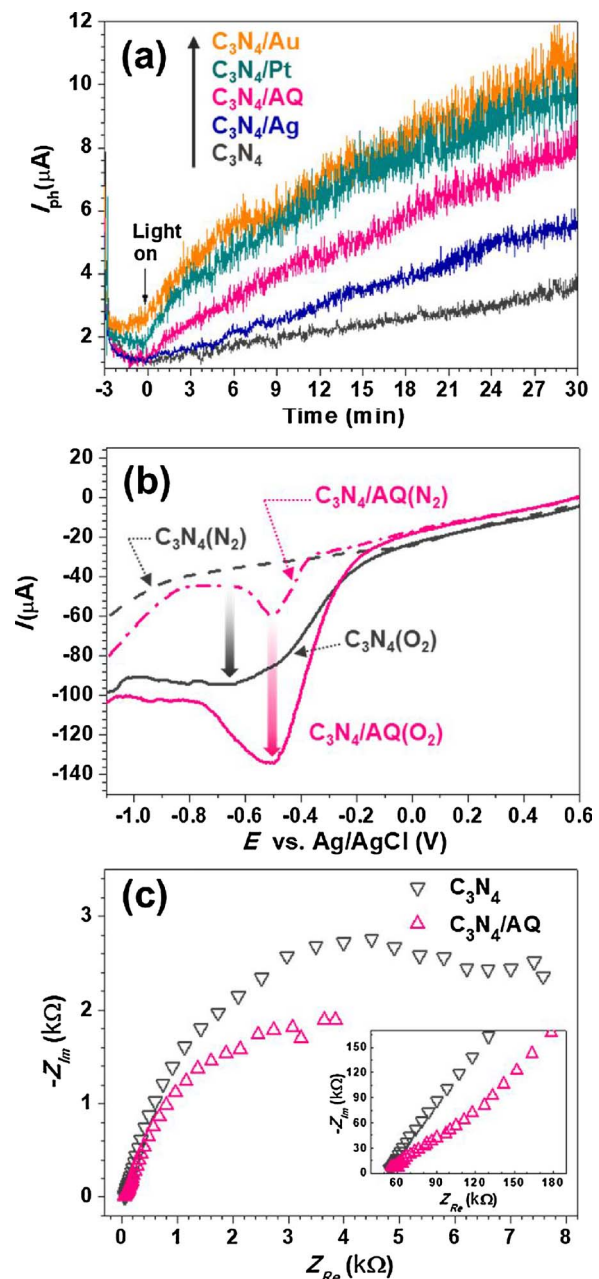


Fig. 5. (a) Time-profiles of Fe³⁺-mediated photocurrent collected on a Pt electrode in the aqueous suspension of C₃N₄, C₃N₄/AQ(-COOH) (10 wt%), and C₃N₄/(Ag, Au, Pt) metals (1 wt%). The experimental conditions were as follows: [catalyst] = 0.5 g L⁻¹, [Fe³⁺] = 2.0 mM, [NaClO₄] = 0.1 M, pH_i = 1.8, 100 mW cm⁻² (AM 1.5), Pt electrode held at +0.8 V (vs Ag/AgCl), and under N₂-pursing. (b) LSV curves of C₃N₄ and C₃N₄/AQ (-COOH) (10 wt%) electrodes in 0.5 M (pH = 7.0) phosphate buffer solution at a scan rate of 50 mV s⁻¹ under N₂- or O₂-pursing (without light). (c) Nyquist plots of C₃N₄ and C₃N₄/AQ(-COOH) (10 wt%) electrodes were obtained in the range from 0.5 Hz to 100 kHz at a representative potential of -0.5 V (vs. Ag/AgCl) under O₂-saturated condition, in 0.5 M (pH = 7.0) phosphate buffer solution (without light). The inset in (c) shows magnified Nyquist plots at the higher frequency range.

conclusion that the incorporation of AQ plays an essential role in H₂O₂ production by accelerating formation kinetics and decelerating decomposition kinetics for H₂O₂.

3.4. Photoelectrochemical and electrochemical analyses

We were able to further verify the role of AQ as an electron-withdrawing co-catalyst by measuring a photo-generated current, collected

by the $\text{Fe}^{3+}/\text{Fe}^{2+}$ redox shuttle, in a $\text{C}_3\text{N}_4/\text{AQ}$ suspension under simulated solar irradiation (Fig. 5a) [61]. Compared to bare C_3N_4 , the $\text{C}_3\text{N}_4/\text{AQ}$ exhibited significantly increased photocurrent during light irradiation, which is comparable to those of noble metal-loaded C_3N_4 composites. The photocurrent generation during the 30 min reaction (I_{ph} at 30 min – I_{ph} at 0 min) was 8.21 μA for $\text{C}_3\text{N}_4/\text{Au}$, 7.94 μA for $\text{C}_3\text{N}_4/\text{Pt}$, 6.82 μA for $\text{C}_3\text{N}_4/\text{AQ}$, 4.28 μA for $\text{C}_3\text{N}_4/\text{Ag}$, and 2.29 μA for bare C_3N_4 , respectively. The Pt wire working electrode was poised at 1.1 V vs. RHE (0.8 V vs. Ag/AgCl), oxidizing Fe^{2+} back to Fe^{3+} at an effective anodic current. The relatively sluggish photocurrent generation on $\text{C}_3\text{N}_4/\text{Ag}$ is due to the slow interfacial electron transfer that occurred on Ag rather than other noble metals [62]. The back reaction of C_3N_4 absorbers oxidizing Fe^{2+} back to Fe^{3+} may occur, reducing the effective anodic currents on an equal basis. The result indicates that AQ functions to separate charges of C_3N_4 and transfer electrons to the Fe^{3+} redox shuttles in a way similar to how noble metal co-catalysts function.

The charge separated by AQ further contributes to oxygen reduction, as further verified by electrochemical potential sweep measurements performed using photocatalyst-loaded GCE under N_2 and O_2 saturated conditions. The CV curve of C_3N_4 in Fig. S10a displayed a rectangular shape (the electrical double-layer capacitance) without any peaks under N_2 saturated condition, whereas a pair of redox peaks was observed at around –0.46 V vs. Ag/AgCl (–0.51 V_{Ag/AgCl} for the cathodic peak and –0.42 V_{Ag/AgCl} for the anodic peak) on $\text{C}_3\text{N}_4/\text{AQ}$ (Fig. S10b). These redox peaks correspond to the aforementioned hydrogenation (AQ to AQH_2) and dehydrogenation (AQH_2 to AQ) reactions [26] in Scheme 1. In LSV (Fig. 5b), a large increase in the oxygen reduction current along with a reduction peak potential (shifted from –0.66 V_{Ag/AgCl} for C_3N_4 to –0.50 V_{Ag/AgCl} for $\text{C}_3\text{N}_4/\text{AQ}$) under an O_2 saturated condition with $\text{C}_3\text{N}_4/\text{AQ}$ also indicates that AQ facilitates the oxygen reduction by utilizing AQ chemistry. It is noteworthy that $\text{C}_3\text{N}_4/\text{AQ}$ exhibited even greater oxygen reduction activity than $\text{C}_3\text{N}_4/\text{Au}$, the noble metal with the highest H_2O_2 production potential, with respect to both the oxygen reduction current and the reduction peak potential (Fig. S10c).

The results of EIS analyses, shown as Nyquist plots in Fig. 5c and bode plots in Fig. S11, consistently point toward the occurrence of AQ chemistry in Scheme 1 in our system. The C_3N_4 electrode resulted in a large hemisphere in the Nyquist plot that fit well to a single-capacitance Randles circuitry. In contrast, the $\text{C}_3\text{N}_4/\text{AQ}$ electrode exhibited two incomplete hemispheres with data fitting to a double-capacitance Randles circuitry. The result is likely to have come from the involvement of two-step reactions: the first capacitive arc from the reaction leading to the formation of AQH_2 by the hydrogenation of AQ, and the second capacitive arc from the reaction AQH_2 with O_2 to form H_2O_2 . In addition, the total resistance of $\text{C}_3\text{N}_4/\text{AQ}$, the sum of R_{CT1} (for AQH_2 formation) and R_{CT2} (for H_2O_2 production), was much smaller than that ($R_{\text{CT(total)}}$) of C_3N_4 (Fig. S11 table). The PEC/EC results above confirm the involvement of AQ chemistry for H_2O_2 production when composited with C_3N_4 .

3.5. H_2O_2 Production by melem/AQ composite

We further confirmed the role of AQ in photocatalytic H_2O_2 production by attaching AQ on melem, a subunit of C_3N_4 . Melem's photocatalytic property is analogous to that of C_3N_4 but with greater bandgap energy [33,63]. The ending amine groups on melem can also be combined with the AQ-COOH in the same way as with C_3N_4 and AQ (-COOH). The results from FT-IR and XPS showed that attaching AQ to melem results in characteristic changes similar to those resulting from attaching AQ to C_3N_4 (Fig. S12).

The trend with melem was similar to that with C_3N_4 : incorporating AQ onto melem increased H_2O_2 production (Fig. 6a) due to 4-times higher formation rate constant (from 1.03 $\mu\text{mol g}^{-1}\text{min}^{-1}$ to 4.49 $\mu\text{mol g}^{-1}\text{min}^{-1}$) and a 2-times smaller decomposition rate

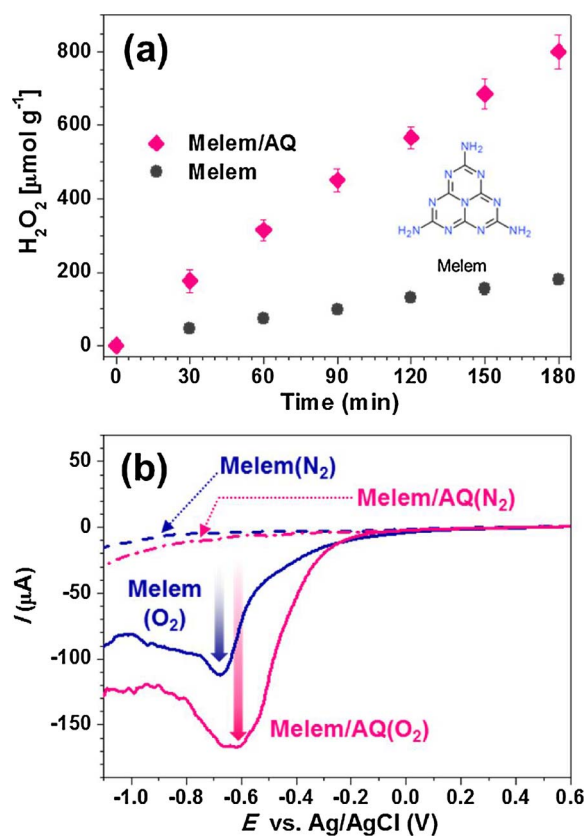


Fig. 6. (a) Time-dependent profiles of H_2O_2 production by melem and melem/AQ (-COOH) (10 wt%). The experimental conditions were as follows: [catalyst] = 0.5 g L^{-1} , [2-propanol]₀ = 10 vol%, pH_i = not adjusted, 100 mW cm^{-2} (AM 1.5), and O_2 -saturated. (b) LSV curves of melem and melem/AQ(-COOH) (10 wt%) electrodes in 0.5 M (pH = 7.0) phosphate buffer solution at a scan rate of 50 mV s^{-1} under N_2 - or O_2 -purging (without light).

constant (from 0.0006 min^{-1} to 0.0003 min^{-1}). The results of PEC analyses, performed following the same procedure, led to the same conclusion: AQ functions as a co-catalyst (Figs. 6b and S13). The melem/AQ combination has a much lower H_2O_2 production than $\text{C}_3\text{N}_4/\text{AQ}$ and therefore will not be an optimal choice, but this set of data once again confirms the unique, significant role of AQ chemistry at work.

3.6. Quantum yields and repeated use

Fig. 7 shows the apparent quantum yield (AQY) for the H_2O_2 production by C_3N_4 and $\text{C}_3\text{N}_4/\text{AQ}$ as a function of the incident monochromatic light. The AQY profile of $\text{C}_3\text{N}_4/\text{AQ}$ closely resembles its absorption spectrum and was consistently higher than that of C_3N_4 . We observed as much as an 8.3-fold enhancement under the monochromatic irradiation at 380 nm (19.5% for $\text{C}_3\text{N}_4/\text{AQ}$ and 2.3% for C_3N_4).

Integrating the AQY spectral response with the AM 1.5 solar spectrum yields an estimated H_2O_2 production rate of 323.1 $\mu\text{mol g}^{-1}\text{h}^{-1}$ under 1-sun illumination (diameter of a circular illumination spot at ca. 2 cm), which is consistent with the H_2O_2 amount quantified experimentally. The observation that the AQY profile mirrored the absorption spectrum suggests that our photocatalyst geometry has been optimized for efficient optical absorption and charge collections. However, the observation that the charge collection leading to selective H_2O_2 production only reached a 20% efficiency, far from 100%, suggests the existence of additional futile recombination pathways. Further optimization of $\text{C}_3\text{N}_4/\text{AQ}$ systems to reduce their charge or product recombination is needed.

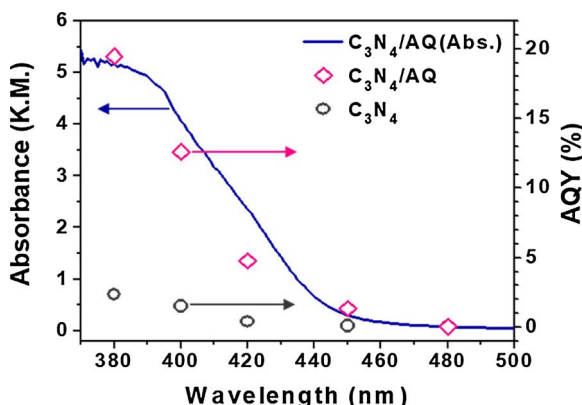


Fig. 7. (a) Absorption spectrum (left axis) and (b) apparent quantum yield (AQY, right axis) of the photocatalytic H₂O₂ production as a function of wavelength on C₃N₄/AQ (10 wt%). The experimental conditions were as follows: [catalyst] = 1 g L⁻¹, [2-propanol]₀ = 10 vol%, pH_i = not adjusted, O₂-saturated.

4. Conclusions

We have successfully demonstrated that AQ chemistry, a central mechanism that accounts for efficient and selective H₂O₂ production in industrial catalytic processes, can be readily exploited to significantly enhance photocatalytic H₂O₂ production when coupled with C₃N₄ photocatalysts under simulated 1-sun illumination with either water or organics as an electron donor. The AQ-augmented C₃N₄ (10% wt) reached an optimal H₂O₂ production rate of 361 μmol g⁻¹ h⁻¹ under simulated 1-sun illumination. Compared to commonly used co-catalysts such as Ag, Au, Pt, C₆₀, and (r)GO, AQ was found to be more selective at promoting 2-electron O₂ reduction to H₂O₂ and suppressing decomposition of produced H₂O₂. This selectivity resulted from the unique roles of AQ as a co-catalyst that (i) effectively accepts electrons from the CB of excited C₃N₄ and (ii) utilizes the electrons to initiate two-step H₂O₂ synthesis (hydrogenation: AQ + 2H⁺ + 2e⁻ → AQH₂; dehydrogenation: AQH₂ + O₂ → AQ + H₂O₂). Successful demonstration with C₃N₄ suggests the possibility of other photocatalysts and photoelectrodes to achieve a similar result. For example, if a photoelectrode loaded with C₃N₄/AQ were assumed to follow the same AQY profile, we estimate that the equivalent photocurrent density would reach 0.165 mA cm⁻², or 0.178% solar-to-fuel conversion efficiency. Note that a water-splitting photocatalyst suspension of single-absorber SrTiO₃:Rh,Sb (Rh and Sb co-doped) particles with IrO₂ co-catalysts recently showed a ~0.1% solar-to-fuel conversion efficiency [64,65]. We expect that further improvement in H₂O₂ production can be achieved by (i) varying the relative positions of the redox potential of AQ/AQH₂ and the band edge positions of semiconductor absorbers with respect to O₂/H₂O₂ potentials, (ii) anchoring AQ to photocatalysts with broader visible-light absorption spectra, and (iii) developing theoretical predictive models to optimize the absorbers/co-catalysts combination.

Acknowledgements

This work was supported by the National Science Foundation (CBET-1335934), Basic Science Research Program (NRF-2017R1A2B2008952) funded by the Korean government (MSIP) through NRF, and by the Yonsei University Future-leading Research Initiative of 2017 (2017-22-0043). S.H. thanks the Energy Sciences gift fund from the TomKat Foundation to Yale University.

Appendix A. Supplementary data

Supplementary material related to this article can be found, in the online version, at doi:<https://doi.org/10.1016/j.apcatb.2018.01.060>.

References

- [1] United Nation International Commodities Data, United Nations, 2016.
- [2] J.M. Campos-Martin, G. Blanco-Brieva, J.L.G. Fierro, Angew. Chem. Int. Ed. 45 (2006) 6962–6984.
- [3] T.T.M. Nguyen, H.J. Park, J.Y. Kim, H.E. Kim, H. Lee, J. Yoon, C. Lee, Environ. Sci. Technol. 47 (2013) 13661–13667.
- [4] G. Ruppert, R. Bauer, Chemosphere 28 (1994) 1447–1454.
- [5] M.A. Ak, A. Ulas, B. Sumer, B. Yazici, C. Yildirim, L.O. Gonc, F.E. Orhan, Fuel 90 (2011) 395–398.
- [6] A.E. Sanli, A. Aytac, Int. J. Hydrogen Energy 36 (2011) 869–875.
- [7] S.-i. Yamazaki, Z. Siroma, H. Senoh, T. Ioroi, N. Fujiwara, K. Yasuda, J. Power Sources 178 (2008) 20–25.
- [8] Y. Yamada, M. Yoneda, S. Fukuzumi, Energ. Environ. Sci. 8 (2015) 1698–1701.
- [9] G.H. Moon, W. Kim, A.D. Bokare, N.E. Sung, W. Choi, Energ. Environ. Sci. 7 (2014) 4023–4028.
- [10] H.-i. Kim, O.S. Kwon, S. Kim, W. Choi, J.-H. Kim, Energ. Environ. Sci. 9 (2016) 1063–1073.
- [11] H.-J. Riedl, G. Pfleiderer, 1939. Production of hydrogen peroxide, in: I.G.F. AG. (Ed.), [Chem. Abstr. 1939, 33, 49 337], C01B15/023 ed., (I. G. Farbenindustrie AG.).
- [12] D. Hanuc, H. Green, E.J. Beckman, Ind. Eng. Chem. Res. 41 (2002) 4466–4474.
- [13] G. Centi, S. Perathoner, S. Abate, N. Mizuno (Ed.), Direct Synthesis of Hydrogen Peroxide: Recent Advances, Wiley-VCH, Weinheim, 2009.
- [14] N.M. Wilson, D.W. Flaherty, J. Am. Chem. Soc. 138 (2016) 574–586.
- [15] Y. Wang, X.C. Wang, M. Antonietti, Angew. Chem. Int. Ed. 51 (2012) 68–89.
- [16] C.A. Paez, D.Y. Liquet, C. Calberg, S.D. Lambert, I. Willems, A. Germeau, J.P. Pirard, B. Heinrichs, Catal. Commun. 15 (2011) 132–136.
- [17] J. Liu, Y. Liu, N.Y. Liu, Y.Z. Han, X. Zhang, H. Huang, Y. Lifshitz, S.T. Lee, J. Zhong, Z.H. Kang, Science 347 (2015) 970–974.
- [18] Y. Shiraishi, S. Kanazawa, Y. Sugano, D. Tsukamoto, H. Sakamoto, S. Ichikawa, T. Hirai, ACS Catal. 4 (2014) 774–780.
- [19] G.H. Moon, M. Fujitsuka, S. Kim, T. Majima, X.C. Wang, W. Choi, ACS Catal. 7 (2017) 2886–2895.
- [20] M.V. Dozzi, L. Prati, P. Canton, E. Selli, Phys. Chem. Chem. Phys. 11 (2009) 7171–7180.
- [21] D. Tsukamoto, A. Shiro, Y. Shiraishi, Y. Sugano, S. Ichikawa, S. Tanaka, T. Hirai, ACS Catal. 2 (2012) 599–603.
- [22] M. Piccinini, E. Ntaijinja, J.K. Edwards, A.F. Carley, J.A. Moulijn, G.J. Hutchings, Phys. Chem. Chem. Phys. 12 (2010) 2488–2492.
- [23] W.C. Wan, S. Yu, F. Dong, Q. Zhang, Y. Zhou, J. Mater. Chem. A 4 (2016) 7823–7829.
- [24] Q.J. Xiang, J.G. Yu, M. Jaroniec, J. Phys. Chem. C 115 (2011) 7355–7363.
- [25] Y. Zheng, L.H. Lin, B. Wang, X.C. Wang, Angew. Chem. Int. Ed. 54 (2015) 12868–12884.
- [26] I. Tiwari, M. Gupta, R. Prakash, C.E. Banks, Anal. Methods 6 (2014) 8793–8801.
- [27] C.L. Allen, A.R. Chhatwal, J.M. Williams, Chem. Commun. 48 (2012) 666–668.
- [28] H. Park, W. Choi, M.R. Hoffmann, J. Mater. Chem. 18 (2008) 2379–2385.
- [29] X.J. Bai, L. Wang, Y.J. Wang, W.Q. Yao, Y.F. Zhu, Appl. Catal. B 152 (2014) 262–270.
- [30] D.C. Marcano, D.V. Kosynkin, J.M. Berlin, A. Sinitskii, Z.Z. Sun, A. Slesarev, L.B. Alemany, W. Lu, J.M. Tour, Acs Nano 4 (2010) 4806–4814.
- [31] G.M. Eisenberg, Ind. Eng. Chem. 15 (1943) 327–328.
- [32] H. Bader, V. Sturzenegger, J. Hoigne, Water Res. 22 (1988) 1109–1115.
- [33] B. Jürgens, E. Irran, J. Senker, P. Kroll, H. Müller, W. Schnick, J. Am. Chem. Soc. 125 (2003) 10288–10300.
- [34] P.X. Qiu, H. Chen, C.M. Xu, N. Zhou, F. Jiang, X. Wang, Y.S. Fu, J. Mater. Chem. A 3 (2015) 24237–24244.
- [35] J. Tauc, R. Grigorovici, A. Vancu, Phys. Stat. Sol. 15 (1966) 627–637.
- [36] M.J. Bojdys, J.O. Muller, M. Antonietti, A. Thomas, Chem. Eur. J. 14 (2008) 8177–8182.
- [37] S. Martha, A. Nashim, K.M. Parida, J. Mater. Chem. A 1 (2013) 7816–7824.
- [38] M. Xu, L. Han, S.J. Dong, ACS Appl. Mater. Interfaces 5 (2013) 12533–12540.
- [39] M. Higo, T. Miake, M. Mitsushio, T. Yoshidome, Y. Ozono, Anal. Sci. 24 (2008) 313–320.
- [40] M. Srivastava, S.K. Srivastava, N.R. Nirala, R. Prakash, Anal. Methods 6 (2014) 817–824.
- [41] H.S. Randhawa, J.L. Kapoor, J. Comput. Chem. 2 (1981) 12–13.
- [42] W. Chen, L.J. Huang, J. Hu, T.F. Li, F.F. Jia, Y.F. Song, Phys. Chem. Chem. Phys. 16 (2014) 19668–19673.
- [43] B.V. Lotsch, M. Doblinger, J. Sehnert, L. Seyfarth, J. Senker, O. Oeckler, W. Schnick, Chem. Eur. J. 13 (2007) 4969–4980.
- [44] Q. Huang, J.G. Yu, S.W. Cao, C. Cui, B. Cheng, Appl. Surf. Sci. 358 (2015) 350–355.
- [45] S.W. Han, S.W. Joo, T.H. Ha, Y. Kim, K. Kim, J. Phys. Chem. B 104 (2000) 11987–11995.
- [46] C. Goel, H. Bhunia, P.K. Bajpai, RSC Adv. 5 (2015) 46568–46582.
- [47] B.C. Zhu, P.F. Xia, W.K. Ho, J.G. Yu, Appl. Surf. Sci. 344 (2015) 188–195.
- [48] Q. Su, J. Sun, J.Q. Wang, Z.F. Yang, W.G. Cheng, S.J. Zhang, Catal. Sci. Technol. 4 (2014) 1556–1562.
- [49] S. Samanta, S. Martha, K. Parida, Chemcatchem 6 (2014) 1453–1462.
- [50] Z. Li, B. Tian, W. Zhang, X. Zhang, Y. Wu, G. Lu, Appl. Catal., B. 204 (2017) 33–42.
- [51] B. Chai, X. Liao, F.K. Song, H. Zhou, Dalton Trans. 43 (2014) 982–989.
- [52] Y.B. Li, H.M. Zhang, P.R. Liu, D. Wang, Y. Li, H.J. Zhao, Small 9 (2013) 3336–3344.
- [53] H.I. Kim, G.H. Moon, D. Monllor-Satoca, Y. Park, W. Choi, J. Phys. Chem. C 116 (2012) 1535–1543.
- [54] H.-i. Kim, S. Kim, J.K. Kang, W. Choi, J. Catal. 309 (2014) 49–57.

- [55] N. An, F.H. Zhang, Z.G. Hu, Z.M. Li, L. Li, Y.Y. Yang, B.S. Guo, Z.Q. Lei, Rsc Adv. 5 (2015) 23942–23951.
- [56] J.N. Moore, D. Phillips, N. Nakashima, K. Yoshihara, J. Chem. Soc. Farad. 82 (1986) 745–761.
- [57] A. Sarapuu, K. Vaik, D.J. Schiffrin, K. Tammeveski, J. Electroanal. Chem. 541 (2003) 23–29.
- [58] A.J. Hoffman, E.R. Carraway, M.R. Hoffmann, Environ. Sci. Technol. 28 (1994) 776–785.
- [59] C. Kormann, D.W. Bahnemann, M.R. Hoffmann, Environ. Sci. Technol. 22 (1988) 798–806.
- [60] A.J. Bard, R. Parsons, J. Jordan, Standard Potentials in Aqueous Solution, Taylor & Francis, London, 1985.
- [61] H. Park, W. Choi, J. Phys. Chem. B 108 (2004) 4086–4093.
- [62] Y. Choi, H.I. Kim, G.H. Moon, S. Jo, W. Choi, ACS Catal. 6 (2016) 821–828.
- [63] X.Q. Wei, Y. Qiu, W.Y. Duan, Z.X. Liu, RSC Adv. 5 (2015) 26675–26679.
- [64] R. Asai, H. Nemoto, Q. Jia, K. Saito, A. Iwase, A. Kudo, Chem. Commun. 50 (2014) 2543–2546.
- [65] D.M. Fabian, S. Hu, N. Singh, F.A. Houle, T. Hisatomi, K. Domen, F.E. Osterloh, S. Ardo, Energ. Environ. Sci. 8 (2015) 2825–2850.